Characterization of fatigue crack of hydrogen-charged austenitic stainless steel by electromagnetic and ultrasonic techniques

Sho Takeda, Yoshikazu Ohara, Tetsuya Uchimoto, Hirotoshi Enoki, Takashi Iijima, Eri Tokuda, Takumi Yamada, Yuzo Nagatomo

Characterization of Fatigue Crack of Hydrogen-Charged Austenitic Stainless Steel by Electromagnetic and Ultrasonic Techniques

Sho Takeda[a], Yoshikazu Ohara[b], Tetsuya Uchimoto[ac], Hirotoshi Enoki[d], Takashi Iijima[d], Eri Tokuda[ae], Takumi Yamada[b], Yuzo Nagatomo[b]*

[a]Institute of Fluid Science, Tohoku University, 2-1-1 Katahira, Aoba-ku, Sendai, Miyagi, 980-8577, Japan

[b]Department of Materials Processing, Tohoku University, 6-6-02 Aoba, Aramaki-aza, Aoba-ku, Sendai, Miyagi 980-8579, Japan

[c]CNRS - UDL - TOHOKU University, UMI ELyTMaX, Sendai, Japan

[d]National Institute of Advanced Industrial Science and Technology, 16-1 Onogawa, Tsukuba, Ibaraki, 305-8569, Japan

[e]Graduate School of Engineering, Tohoku University, 6-6 Aramaki Aza Aoba, Aoba-ku, Sendai, Miyagi, 980-8579, Japan

**Corresponding author.*
Email address: uchimoto@tohoku.ac.jp

Abstract

In this study, the feasibility of the fusion sensing of eddy current testing (ECT) and ultrasonic testing (UT) as effective tools to clarify the hydrogen-embrittlement mechanism of austenitic stainless steels was investigated. Fatigue testing was conducted on hydrogen-charged and uncharged AISI 304 specimens. The effect of hydrogen exposure on the martensitic phase transformation, and crack closure and crack face morphology were investigated by ECT and UT. The results suggest that a comparison of ECT and UT results can evaluate martensite transformation and crack closure and crack face morphology, which are important in understanding the hydrogen embrittlement of austenitic stainless steels.

Keywords: Fusion of eddy current testing and ultrasonic testing; Hydrogen embrittlement; Fatigue crack growth; Martensitic transformation; Crack closure

Highlights

- Effect of hydrogen on austenitic stainless steels during fatigue testing was investigated by eddy current testing (ECT) and ultrasonic testing (UT).
- Comparison of ECT signals with EBSP analysis for the martensitic transformation.
- Comparison of ECT and UT results for crack closure and crack face morphology investigation.
- It was suggested that a comparison of the ECT and UT results can evaluate the martensite transformation and the crack closure and crack face morphology.

1. Introduction

Hydrogen has received attention as a carbon-free energy carrier, and may serve as an electricity alternative to conventional fossil fuels [1]. In practice, hydrogen embrittlement is an important issue for safety and reliability. Hydrogen embrittlement is a material deterioration phenomenon that is caused by atomic hydrogen penetration into the metal lattice [2].

One of the simplest and most effective ways to prevent hydrogen embrittlement is to use materials with a high hydrogen-embrittlement resistance. For instance, austenitic stainless steels are used extensively in hydrogen station piping [3]. However, embrittlement still occurs in austenitic stainless steels, and many attempts have been made to elucidate the mechanisms to ensure the system safety and reliability.

As for other physical material phenomena, the mechanisms of hydrogen embrittlement of austenitic stainless steels have been investigated at various scales, ranging from the effect of hydrogen atoms on the metal crystal lattice to macroscopic fracture phenomena. Among them, fatigue fracture is most important for practical application. Hydrogen reduces the fatigue strength of materials. It is also used mainly in a compressed gaseous state because of its boiling point, and repeated loading and unloading cycles occur inside the piping. Therefore, the most important failure phenomenon that should be

considered in practical use of austenitic stainless steels as hydrogen components is fatigue failure [4].

Previous studies have shown that the martensitic transformation and crack face morphology are important with regards the effect of hydrogen on the fatigue failure of austenitic stainless steels.

For martensitic transformation, the effect of hydrogen on the fatigue properties of austenitic stainless steels is correlated with the austenite stability and other properties, such as tensile strength. A higher Ni equivalent ratio in the material results in a higher austenite stability and a reduced effect of hydrogen on the fatigue strength [3] [4] [5] [6] [7]. During fatigue crack growth, partial martensitic transformation occurs at the fatigue crack tip, and hydrogen is concentrated at the crack tip. This behavior is related to the difference in hydrogen diffusion rate between the martensite and austenite phases [4].

For the crack face morphology, a correlation exists between the austenite stability and fracture surface shape, like the correlation between the intergranular stress corrosion crack (SCC) susceptibility and the fracture surface. Fracture surfaces of metastable austenitic stainless steels, such as AISI304 with hydrogen show a quasi-cleavage surface like SCC, whereas those of stable austenitic stainless steels, such as AISI316L, have dimples, even in a hydrogen atmosphere [8].

These results have been clarified by analyzing the strain–stress curves; by surface observations using optical and electron microscopes, fracture surface observations, and microstructural observations; and by analyzing electron backscatter diffraction patterns (EBSP). However, all evaluations are intermittent and, post-testing, the observation scale is limited to the submicron scale, and the EBSP observation area analysis for martensitic transformation is limited to the submillimeter scale. Thus, in-situ analysis or a macroscale monitoring technique with an appropriate resolution is required to track the phenomenon in more detail. We have investigated the feasibility of nondestructive testing as a tool to elucidate the hydrogen-embrittlement mechanism of austenitic stainless steels.

Eddy current testing (ECT) is a nondestructive electromagnetic testing method [9]. ECT is used to detect flaws on materials, but ECT signals are affected by flaws and the material properties, such as the electrical conductivity and permeability. When the austenite phase transforms to the martensite phase, the permeability changes. The martensitic transformation at the crack tip can be evaluated by detecting this change as a change in ECT signal. Previous studies reported that ECT can analyze the electromagnetic properties of materials [9] and the amount of martensite qualitatively [10] [11] [12] [13]. For the crack fracture surface, hydrogen-embrittled austenitic stainless steels exhibit quasi-cleavage fracture surfaces like those of the

intergranular SCC as described above. Because a three-dimensional fracture surface results in a larger contact area, cracks with this type of quasi-cleavage fracture surface exhibit a higher electrical conductivity in the case of crack closure. The types of defects can be modelling by providing more conductivity to the crack region [14] [15].

Another method that has been used extensively to detect and measure cracks nondestructively in laboratory experiments and industrial applications is ultrasonic testing (UT) [16]. The ultrasonic phased array (PA) has attracted attention as an effective UT technique for ultrasonic imaging [17] [18]. Most UT uses ultrasonic scattering that is caused by acoustic impedance mismatch at defects. When an air gap exists between crack faces, ultrasonic scattering occurs because of strong acoustic impedance mismatching between the air and base materials (such as metals) [19]. UT methods are more sensitive to cracks with an air gap than the transformation of austenite into martensite. When crack faces are in contact physically, ultrasonic scattering at cracks is weakened because ultrasound can transmit through the contact parts of the crack faces, which may cause an underestimation and overlooking of closed cracks [20] [21] [22] [23] [24] [25]. This suggest that the crack response intensity can be used to infer the extent of crack closure.

It is well known that UT and ECT complement each other for crack characterization, and multi-sensor based on EMAT and ECT were proposed

[26] [27]. These differences in detection mechanisms suggest that ECT is effective for the martensitic transformation and the comparison of ECT and UT is effective for crack face morphology and crack closure. The hydrogen-embrittlement mechanism of austenitic stainless steels has never been investigated by the multisensor combination of ECT and UT, and an attempt will be made to clarify the hydrogen-embrittlement mechanism from a new perspective.

In this study, austenitic stainless steel AISI 304 was used to prepare hydrogen-charged and uncharged specimens, and fatigue testing was conducted on these specimens. By using ECT and UT on specimens after fatigue testing, the effect of hydrogen exposure on martensitic phase transformation around fatigue cracks and crack closure was investigated. From these experiments, the feasibility of a combination of ECT and UT as effective tools to clarify the hydrogen-embrittlement mechanism of austenitic stainless steels was investigated.

2. Specimen preparation

The compact tension (CT) specimen that was compliant with ASTM-E647 [28] as shown in Fig. 1 was used to obtain fatigue cracks with a constant crack growth rate. The variable *a* in Fig. 1 represents the crack length. The material was solution-treated austenitic stainless steel AISI 304, and its chemical

composition is shown in Table 1.

Four CT specimens were prepared: uncharged and hydrogen-charged specimens with electric discharge machining (EDM) slits (22 mm long, 0.3 mm wide), and uncharged and hydrogen-charged specimens with fatigue crack. The specimens exposed to high-pressure gaseous hydrogen at 100 MPa and 543 K for 300 h to charge hydrogen.

Fatigue testing was conducted at room temperature in ambient atmosphere by using a horizontal testing machine (Lab-5, SHIMADZU). Before the test, a 3.0-mm pre-crack was introduced at a frequency f of 10 Hz, a stress ratio R of 0.1, and a stress intensity factor range ΔK of 20 MPa·m$^{1/2}$. The crack length and stress intensity factor range during the fatigue test were measured by a compliance method by using a crack opening displacement that was obtained by a clip gauge. The crack growth rate was 4.5×10^{-8} and 3.0×10^{-7} m/cycle, respectively. After pre-crack introduction, the fatigue test was conducted at f = 1.0 Hz until the crack length a became 7 mm. The stress ratio R and stress intensity factor range ΔK were varied to compare the effects on the martensitic transformation and crack closure as R = 0.1 and 0.5, and ΔK = 20 and 30 MPa·m$^{1/2}$.

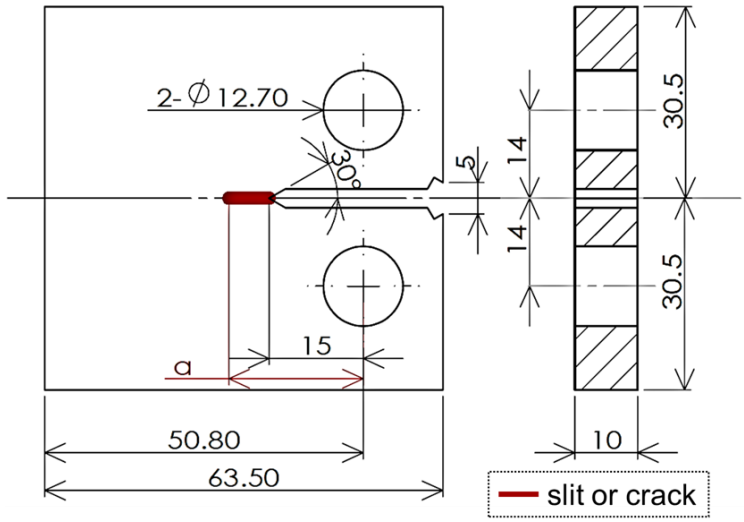

Fig. 1 Schematic illustration of CT specimen.

Table 1 Chemical composition of AISI304 specimen (wt.%).

C	Si	Mn	P	S	Ni	Cr	Co
0.05	0.55	0.94	0.037	0.004	8.07	18.15	0.19

3. Eddy current testing

3.2 Experimental and numerical conditions for ECT

Eddy current testing was conducted on each specimen by using the experimental setup in Fig. 2. A schematic illustration of the pancake-type probe in Fig. 3 was used in the experiment. An additional identical coil was installed above the excitation/pick-up coil for temperature compensation. The

coils had 750 turns, a 2.0-mm inner diameter, a 5.0-mm outer diameter, and a 3.0-mm height. The excitation frequency, peak-to-peak voltage, and lift-off were set to 50 kHz, 0.5 V, and 0.1 mm, respectively. Unidirectional scanning perpendicular to the crack was conducted for each specimen at 2.0 mm from the crack tip. The scanning distance was ± 7.0 mm from the center of the crack, and the scan pitch was 0.1 mm.

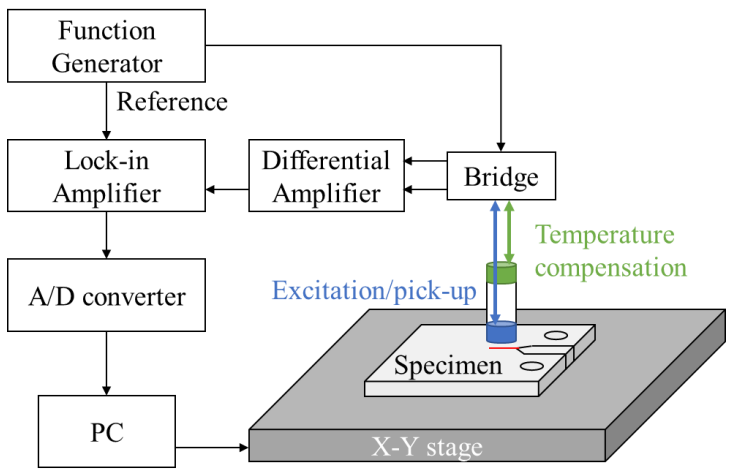

Fig. 2 ECT setup.

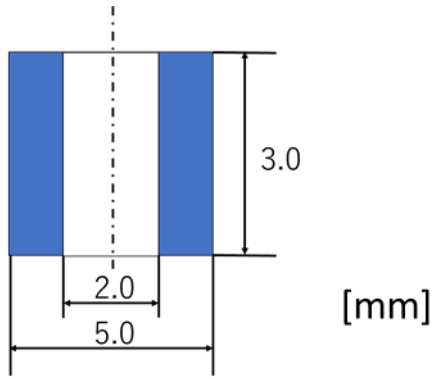

Fig. 3 Pancake coil.

Numerical analysis based on the reduced vector potential method [29] was conducted to analyze the signal change in the experiment. COMSOL Multiphysics® (COMSOL AB) was used for analysis. Figure 4 shows the model that was used in the numerical analysis. The model dimensions were 28 mm × 14 mm × 10 mm. The configuration of the simulation was set to be the same as the experiment. The crack dimensions and electromagnetic parameters of the specimens, such as the relative permeability μ_r and conductivity σ, were changed during the simulation to assess how the ECT signal changes as a function of those factors. The original bulk specimen parameters were $\mu_r = 1.0$ and $\sigma = 1.38 \times 10^6$ S/m. The EDM slit width was set to 0.3 mm based on the EDM wire diameter. The parameters σ and μ_r of the bulk specimens were set to $\mu_r = 1.0$ and $\sigma = 1.38 \times 10^6$ S/m. To model the fatigue cracks, a magnetic phase area was set around the crack faces as shown

in Fig. 5. The magnetic phase width w was set to w = 0.1 mm, and its relative permeability μ_{rm} was changed as μ_{rm} = 1.0 and 6.0 to establish the signal change if martensitic transformation occurred around the fatigue crack. The crack conductivity σ_c was varied as σ_c = 0.1 S/m and 1.5×10^4 S/m to model crack closure. The relative permeability and conductivity of other regions in the specimen were not changed from the EDM specimen model.

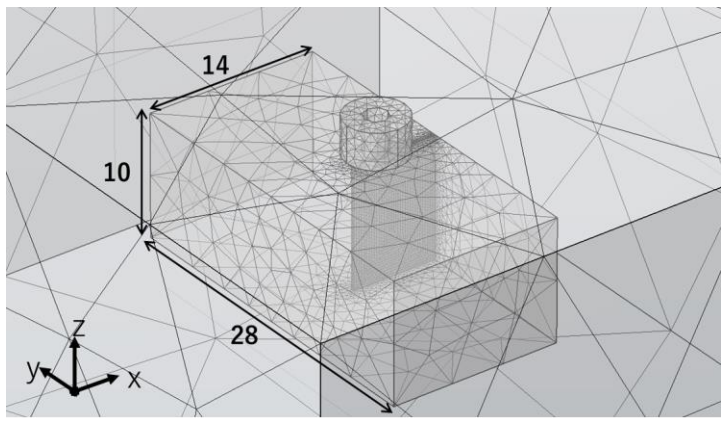

Fig. 4 Numerical model.

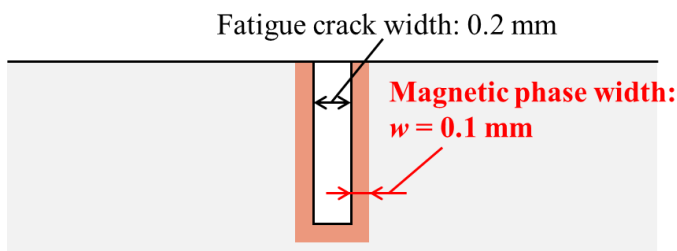

Fig. 5 Numerical analysis setting around fatigue cracks.

3.2 ECT results

The measured ECT signals are shown in Figs. 6 and 7. The maximum amplitude of the obtained ECT signal from the uncharged EDM specimen was set to (V_x, V_y) = (0, 1), and all signals were calibrated from the signal of this specimen. The scanning EDM slit results in Fig. 6 show that no electromagnetic characteristic change was observed after hydrogen charging. Figure 7 shows the signal amplitude and phase change by fatigue testing. Regardless of the testing conditions, ΔK and R, the amplitude of the signal decreased on the hydrogen-charged specimen, and the phase transition was confirmed on the uncharged specimen. The amplitude decrease was more significant in a higher R. The phase transition was more significant at a higher ΔK and R.

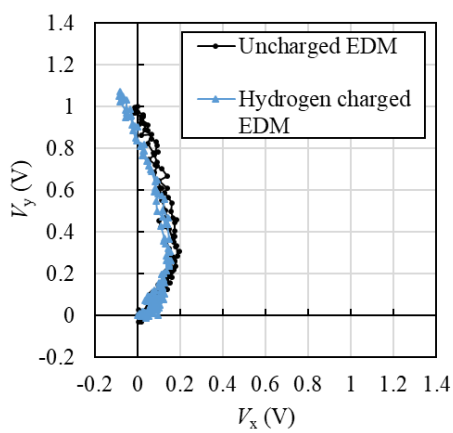

Fig. 6 ECT signals of specimens with EDM slits.

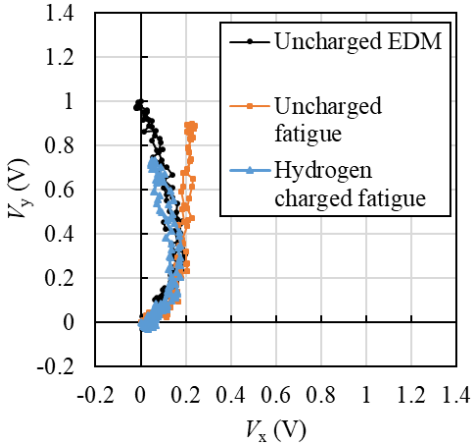

(a) ΔK = 20, R = 0.1.

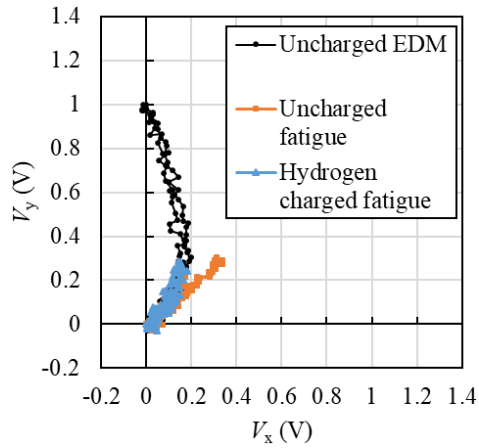

(b) ΔK = 20, R = 0.5.

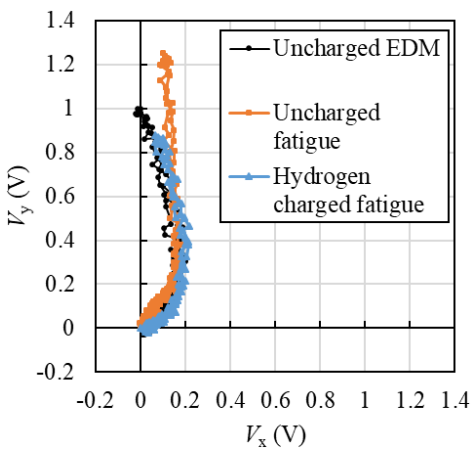

(c) ΔK = 30, R = 0.1.

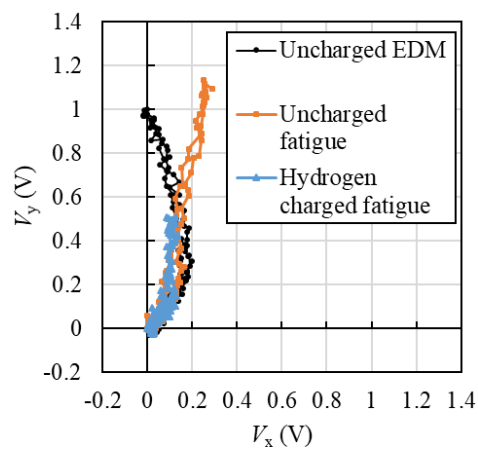

(d) ΔK = 30, R = 0.5.

Fig. 7 ECT signals of specimens after fatigue testings.

Figure 8 shows the numerical result of the scanning EDM slits and fatigue crack on the specimen with different conductivities and relative permeabilities. The EDM slit signal and $\mu_{rm} = 1$ and $\sigma_c = 0.1$ S/m were almost the same and could not be distinguished. This result suggests that the slit width is an insignificant factor in this numerical simulation. If martensitic phase existed around the crack, the amplitude of the ECT signal increased and its phase shifted clockwise. When the crack was closed and the crack surfaces were contacted, the conductivity of the crack region increased and the ECT signal amplitude became small.

A comparison of the numerical and experimental results suggests that martensitic transformation occurred on uncharged specimen, but less transformation occurred on the hydrogen-charged specimen. In contrast, crack closure and contact occurred on the hydrogen-charged specimen. The experimental results show that for larger ΔK and R conditions, a larger phase change was confirmed because the severe stress condition promoted martensitic transformation.

As described in the introduction, crack closure can be detected as a conductivity change, like in the case of SCC. Therefore, it was suggested that the crack closure of fatigue cracks in hydrogen-charged austenitic stainless steel can be evaluated by using ECT.

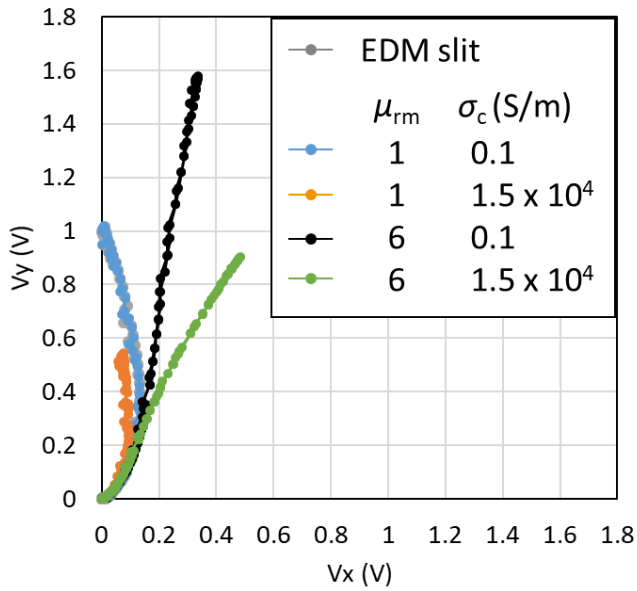

Fig. 8 Numerical analysis results with varied parameters.

4. UT

4.1 Principle of surface-acoustic-wave phased array (SAW PA)

ECT mainly measures the region near the top surface, and so, the use of surface inspection for various UT methods may be appropriate for comparison. One such method is the surface-acoustic-wave phased array (SAW PA) [30] [31] [32]. Unlike typical PAs that use bulk waves, SAW PA uses surface acoustic waves, such as Rayleigh waves. A Rayleigh wave propagates along a surface with a penetration depth of approximately one wavelength. Hence, like ECT, SAW PA that uses Rayleigh waves has a high sensitivity to defects near the surface.

Figure 9 shows a schematic of the SAW PA with Rayleigh waves. To generate Rayleigh waves efficiently, a linear array transducer was placed on a wedge with the critical angle of the Rayleigh wave. The critical angle was calculated from Snell's law:

$$\theta_R = \sin^{-1}\left(\frac{V_{\mathrm{W}}}{V_{\mathrm{R}}}\right) \quad \textbf{(1)}$$

where V_{W} and V_{R} are a longitudinal wave speed in the wedge and a Rayleigh wave speed in the specimen, respectively. A longitudinal wave that was emitted from each element in the array transducer was mode-converted into a Rayleigh wave at the interface between the wedge and specimen. The Rayleigh wave propagates as a leaky Rayleigh wave and Rayleigh wave beneath and outside the wedge, respectively. Both modes are available for SAW PA. The Rayleigh wave outside the wedge is useful for inspection of a large area because the diffraction loss of the Rayleigh wave is smaller than that of the bulk waves [33]. However, transmission losses result at the edge of the wedge upon transmission and reception [30]. The use of a leaky Rayleigh wave beneath the wedge can avoid such transmission losses, which results in a high sensitivity. Hence, we selected the imaging area beneath the wedge in this study. By exciting each element of the array transducer

following the delay law [30] [31] [32], the Rayleigh waves were focused at an arbitrary point on the top surface of the specimen. When defects, such as fatigue cracks, exist near the focal point, Rayleigh wave scattering can occur at the defects. The scattered waves propagate back to each element of the array transducer in a manner opposite to the transmission process. The received waves are processed following a delay-and-sum processing [32] to extract the waves that are scattered at the focal point. The SAW PA that produces a surface image that corresponds to a C-scan image is obtained in real-time by repeating the above process for multiple focal points in the imaging area.

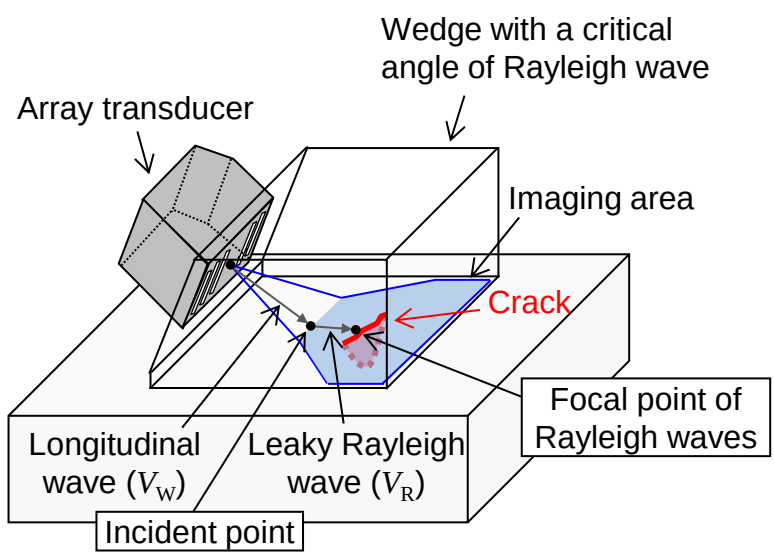

Fig. 9 Principle of SAW PA.

4.2 Experimental conditions

Figure 10 shows the experimental configurations for imaging the fatigue crack by SAW PA. We placed a 32-element linear array transducer (5.0 MHz, 0.5 mm pitch, Imasonic Inc., France) on a polystyrene wedge with the critical angle of a Rayleigh wave. The array transducer was operated by a PA controller (Krautkramer, Japan). The excitation voltage was a pulse wave of 100 V. The sampling rate was 50 MS/s. As shown in Fig. 10, we set the imaging area beneath the wedge to obtain a high sensitivity in the SAW-PA imaging [30]. Over the imaging area, the delay-and-sum processing of the received waves was carried out with steps of 2.0 mm in radius and 1° in angle.

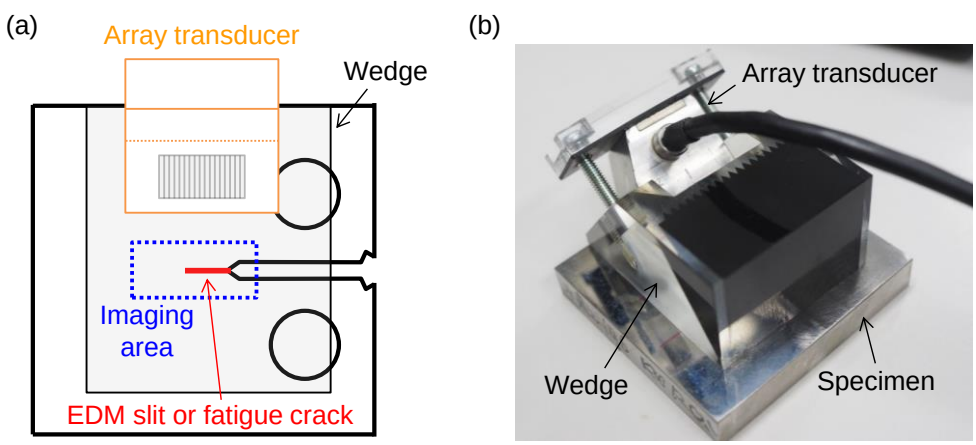

Fig. 10 Experimental configurations for SAW-PA imaging. (a) Schematic illustration. Red lines denote the fatigue crack that formed at the

specimen center. The wedge with the array transducer was positioned above the crack so that the imaging area beneath the wedge contained the fatigue crack. The imaging areas were surrounded by blue dotted lines. (b) Photograph of the array transducer placed on the wedge and the specimen.

4.3 Experimental results

Figure 11(a) shows the SAW-PA image of the uncharged EDM slit specimen. The slit and part of the starting notch were visualized with a high signal-to-noise ratio (SNR). Those positions agreed well with the geometries, which are illustrated schematically in Fig. 11(c). In the hydrogen-charged EDM slit specimen, almost the same image as Fig. 11(a) was obtained, as shown in Fig. 11(b). Therefore, no ultrasonic characteristic change was introduced by the hydrogen charge in the EDM slit specimens.

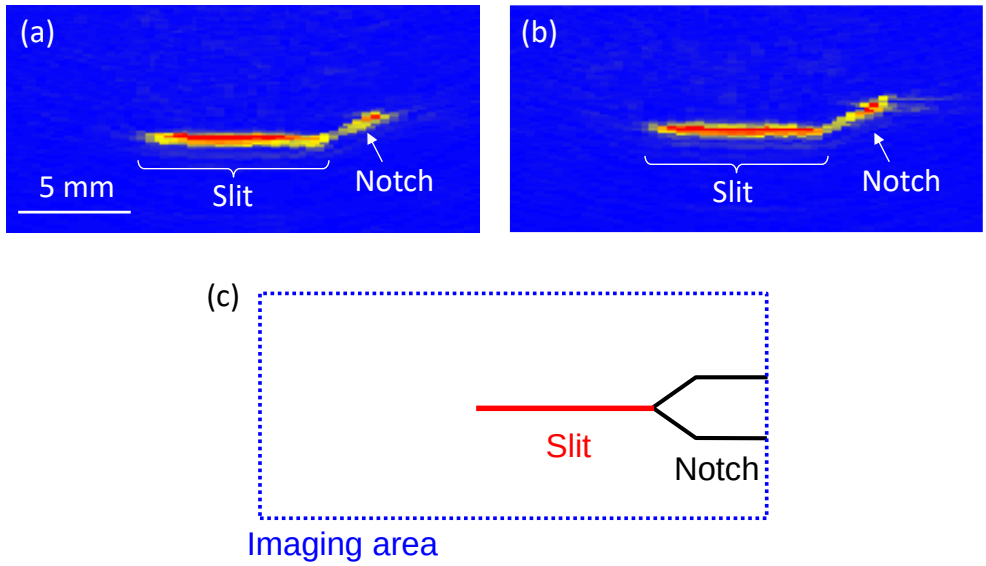

Fig. 11 SAW-PA images of EDM slit specimens. (a) Uncharged specimen. (b) Hydrogen-charged specimen. (c) Schematic illustration of slit in the imaging area.

Figure 12 shows the SAW-PA images of the fatigue crack specimens. In all fatigue-crack specimens, fatigue cracks were visualized at the correct positions in Figs. 12(a)–12(h), as illustrated schematically in Fig. 12(i). The intensities of the crack responses were smaller than those of the slit responses. The intensity distributions were not uniform even within each fatigue crack, which suggests that the fatigue cracks were complexly closed. A detailed description of each imaging result follows.

For the fatigue crack that was produced at ΔK = 20 MPa·m$^{1/2}$ and R = 0.1

in the uncharged specimen, the intensity of the crack response was not uniform in the crack-length direction, as shown in Figs. 12(a). The intensity weakened gradually as the response came closer to the crack tip (i.e., the leftmost edge of the crack). Therefore, the crack was more closed closer to the tip. For the fatigue crack that was produced under the same fatigue condition in the hydrogen-charged austenitic stainless steel, almost the same crack responses as Fig. 12(a) were observed, as shown in Fig. 12(b).

For the fatigue crack that was produced at ΔK = 20 MPa·m$^{1/2}$ and R = 0.5 in the uncharged specimen, the intensities of the crack responses changed markedly at the center of the crack-length direction, as shown in Fig. 12(c). Whereas the intensity of the crack response was strong in the right half, that of the crack response was relatively weak in the left half. This result shows that the crack was open and closed dominantly in the right and left halves, respectively. Here, the right half of the crack was a 3.0-mm pre-crack region and the left half was a fatigue crack region. This result suggests that UT can visualize the difference between the pre-crack and the fatigue crack. For the fatigue crack that was produced under the same fatigue condition in the hydrogen-charged specimen, almost the same crack responses as Fig. 12(c) were observed, as shown in Fig. 12(d).

For the fatigue crack that was produced at ΔK = 30 MPa·m$^{1/2}$ and R = 0.1 in the uncharged specimen, the intensities of the crack responses changed

markedly at the center of the crack-length direction, as shown in Fig. 12(e). The intensity of the crack response was strong in the pre-crack region, whereas that of the crack response was weak in the fatigue crack region. This result shows that the crack was open and closed dominantly in the right and left halves, respectively. This difference arises from the difference between the pre-crack and fatigue crack regions, which is the same as the specimen with ΔK = 20 MPa·m$^{1/2}$ and R = 0.5. For the fatigue crack that was produced at the same fatigue condition in the hydrogen-charged specimen, the responses were weak over the entire crack, as shown in Fig. 12(f). This result shows that the crack was closed. This distribution was like Figs. 12(b). Whereas the intensity in the pre-crack region was stronger in Fig. 12(e) than that in Fig. 12(f), the contrast was opposite in the fatigue crack region.

For the fatigue crack that was produced at ΔK = 30 MPa·m$^{1/2}$ and R = 0.5 in the uncharged specimen, the intensities of most crack responses were strong, except at the region near the crack tip, as shown in Fig. 12(g). This result suggests that the crack tip and other parts were closed and dominantly open, respectively. For the fatigue crack that was produced at the same fatigue condition in the hydrogen-charged specimen, almost the same crack responses as Fig. 12(g) were observed, as shown in Fig. 12(h).

Thus, the imaging results that were obtained by SAW PA clarified the various crack-closure distributions in each specimen. The intensities of the

crack responses near the crack tip can be used to compare the ECT and ultrasonic imaging, which is described in Section 4 to consider the difference in detection mechanism between those methods.

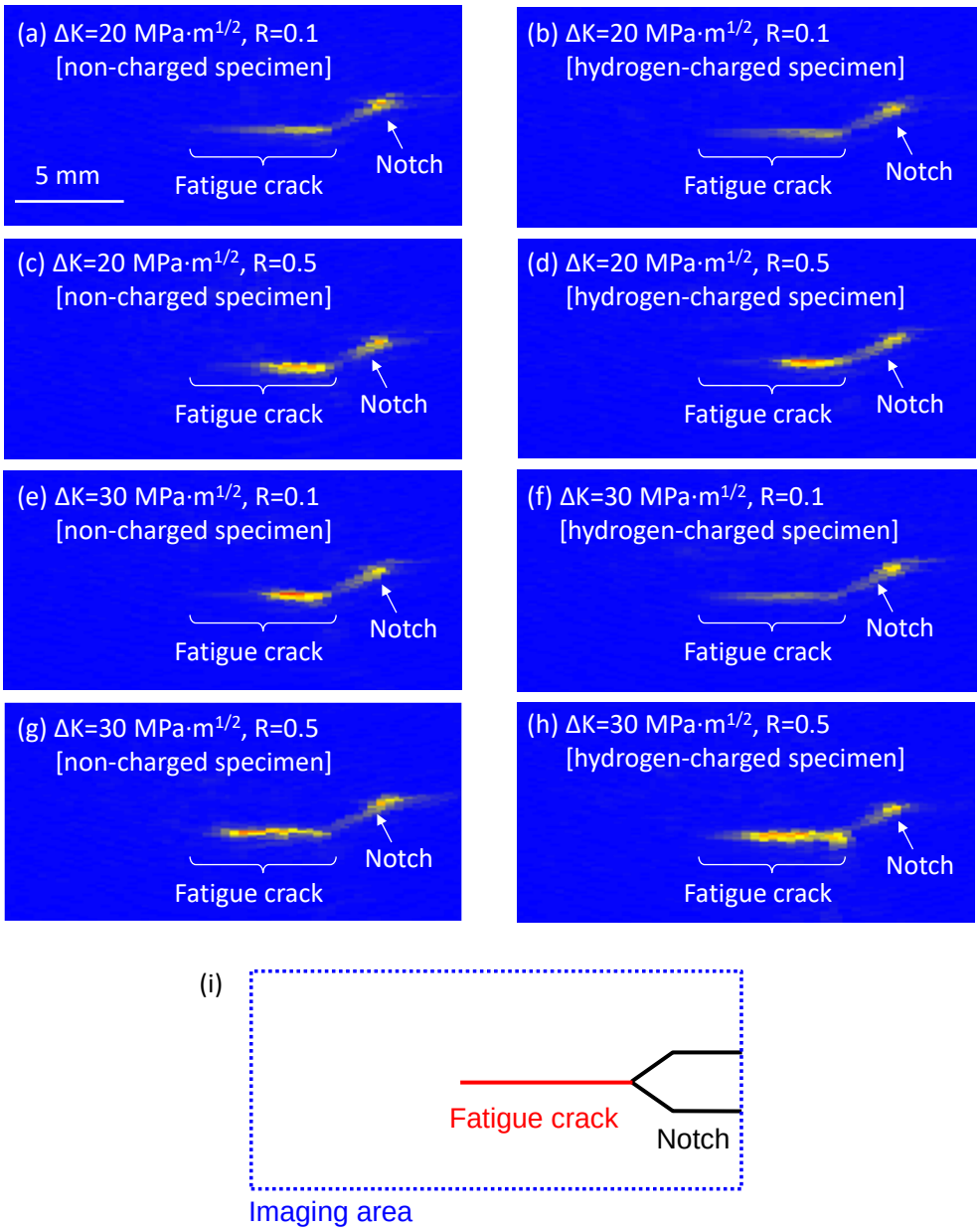

Fig. 12 SAW-PA images of fatigue-crack specimens. (a) and (b) Fatigue cracks produced at $\Delta K = 20$ MPa·m$^{1/2}$ and $R = 0.1$ in uncharged and hydrogen-charged specimens, respectively. (c) and (d) Fatigue cracks produced at $\Delta K = 20$ MPa·m$^{1/2}$ and $R = 0.5$ in uncharged and hydrogen-charged specimens, respectively. (e) and (f) Fatigue cracks produced at $\Delta K = 30$ MPa·m$^{1/2}$ and $R = 0.1$ in uncharged and hydrogen-charged specimens, respectively. (g) and (h) Fatigue cracks produced at $\Delta K = 30$ MPa·m$^{1/2}$ and $R = 0.5$ in uncharged and hydrogen-charged specimens, respectively. (i) Schematic illustration of fatigue crack within the imaging area.

4. Discussion

4.1 Martensitic phase

EBSP analysis was conducted to investigate the martensitic transformation. Figure 13 shows a schematic illustration of the observed EBSP area. An area of 5.0 mm × 5.0 mm × 1.0 mm centered on the crack tip of the specimen was cut out by EDM, and polished mechanically. The specimen was polished by using an Ar-ion polishing machine (PIPS 691, Gatan Inc.). The acceleration voltage and irradiation angle were 4.0 kV and 4°, respectively. Irradiation was carried out for ~30 min to 1 h depending on the surface conditions of the specimens. Four specimens were chosen and

observed: uncharged with $\Delta K = 20$ and 30 and hydrogen-charged with $\Delta K = 20$ and 30. The stress ratio was constant at $R = 0.1$.

Figure 14 shows the EBSP phase mapping of the specimens. Red regions represent the iron α phase and green regions represent the iron γ phase. In the hydrogen-charged specimens, martensitic transformation was hardly observed compared with the uncharged specimens. This result is consistent with the experimental results and previous studies that suggest austenite phase stabilization by hydrogen charging. In the uncharged specimens, the amount of martensite phase increased with an increase in ΔK, which is consistent with the ECT test results. These results suggest that ECT can evaluate the martensitic transformation around fatigue cracks in austenitic stainless steels.

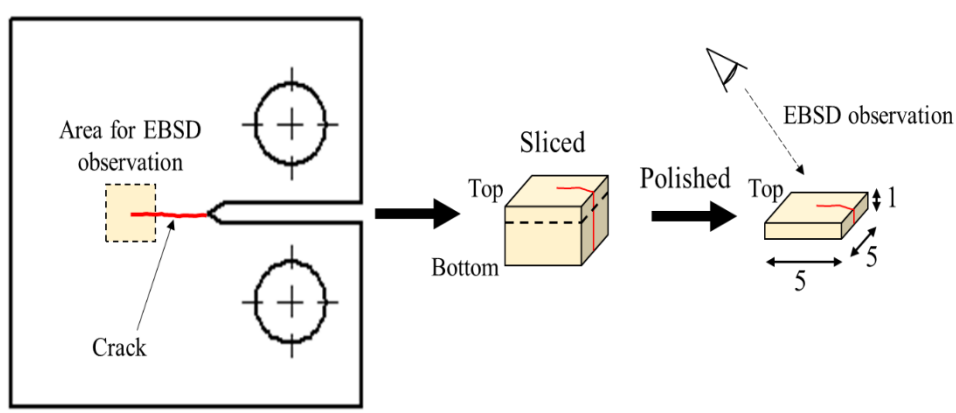

Fig. 13 Schematic illustration of observed area for EBSP.

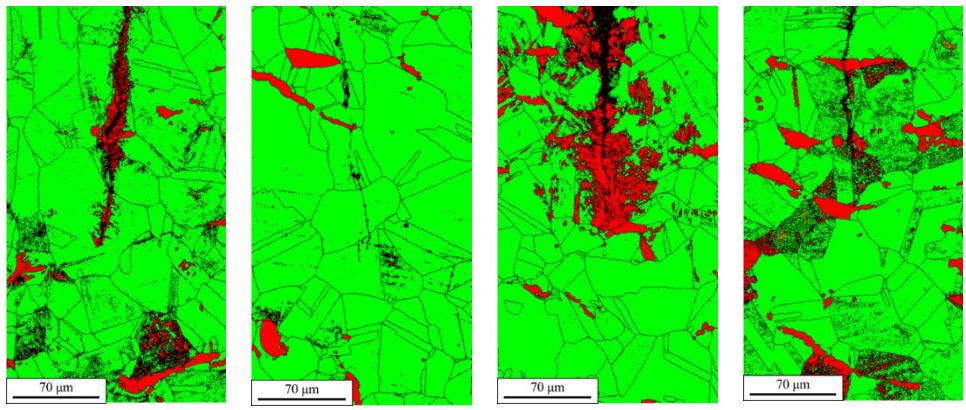

(a) Uncharged ΔK = 20 (b) Hydrogen ΔK = 20 (c) Uncharged ΔK = 30 (d) Hydrogen ΔK = 30

Fig. 14 Schematic illustration of observed area for EBSP.

4.2 Crack closure

To investigate the crack closure, the ECT and UT results were compared and discussed.

The difference between the ECT and UT needed to be considered when comparing the results in the observation area. ECT was used to scan the region 2.0 mm from the crack tip in one dimension, and UT observed almost the entire crack region in two dimensions. Despite this difference, the UT and ECT results agreed well in the same area that was observed by ECT, and each crack in all specimens was closed. The only exception was the uncharged specimen with ΔK = 30 and R = 0.1. For the uncharged sample with ΔK = 30 and R = 0.1, the crack appeared closed according to the UT result but it

appeared open according to the ECT result. This difference appears to be related to the observation area in the depth direction. Although the penetration depth of ECT with an excitation frequency in this study was ~2.0 mm, that of UT was ~0.6 mm. Fatigue cracks tended to lengthen deeper from the specimen surface. Furthermore, crack closure can change depending on the depth of the specimen surface [34]. The difference in crack closure on the uncharged specimen with $\Delta K = 30$ and $R = 0.1$ evaluated by ECT and UT originated from the difference in observation area in the depth direction.

The closure was more pronounced for hydrogen-charged specimens than for uncharged specimens for the same ΔK and R conditions in the ECT results, but the difference by hydrogen charging was not clear in the UT results. For instance, a comparison of Fig. 12(a) and Fig. 12(b) shows no clear change in UT signals before and after hydrogen charging when $\Delta K = 20$ and $R = 0.1$, whereas the ECT signals showed a difference in signal amplitude (see Fig. 7(a)). The difference in observation area in the depth direction mentioned above indicated that the crack closure because of the hydrogen charge was more pronounced in the deeper region than near the specimen surface, based on the difference in the observation area in the depth direction mentioned earlier.

Crack closure in the wider area that could not be observed by ECT is discussed based on the UT result. For the stress ratio R, the crack was more

open in the pre-crack region when R was larger, from a comparison of $\Delta K = 20$, $R = 0.1$ in Fig. 12(a) and $\Delta K = 20$, $R = 0.5$ in Fig. 12(c). For the stress intensity factor range ΔK, specimens with $\Delta K = 20$, $R = 0.5$ in Fig. 12(c) and $\Delta K = 30$, $R = 0.5$ in Fig. 12(g) were compared. Although there was no significant difference in the pre-crack region, the crack appeared to be more open around the center of the crack in the specimen with a larger ΔK. This tendency was confirmed in hydrogen-charged specimens in the comparison of Fig. 12(b) and Fig. 12(d), and Fig. 12(d) and Fig. 12(h). Crack closure is affected by ΔK and R, and the same results were obtained in this study.

From these results, it was suggested that a comparison of the ECT and UT results can evaluate the martensite transformation and the crack closure and crack face morphology, which are important in hydrogen embrittlement of austenitic stainless steels. The difference between the ECT and UT results arises mainly because of the frequency and scanning area rather than these detection mechanisms in this study, but an examination of the experimental conditions that the probe used should allow for a more detailed clarification of the hydrogen-embrittlement mechanism. The results from this study are also expected to be useful for the inspection and monitoring of hydrogen equipment.

5. Concluding remarks

In this study, the feasibility of the combination of ECT and UT as effective tools to clarify the hydrogen-embrittlement mechanism of austenitic stainless steels was investigated. The effect of hydrogen exposure on martensitic phase transformation around fatigue cracks and crack closure of hydrogen-charged austenitic stainless steel fatigue specimens was investigated by ECT and UT. The results are as follows:

(1) The ECT signal change because of the martensitic transformation around the fatigue crack was confirmed especially on the uncharged fatigued specimen and less on the hydrogen-charged specimen. The EBSP analysis was consistent with the ECT results.

(2) Despite the detection mechanism difference, the UT and ECT results agreed well and each crack in all specimens was closed. In some cases, the difference in the results could be confirmed because of the ECT and UT observation areas. UT clarified that the effect of the crack closure is affected by the stress intensity factor range and stress ratio on the area that could not be observed ECT.

Acknowledgements

This work was partly supported by JKA and its promotion funds from KEIRIN RACE (No.158). "Research and development on visualization by

electromagnetic sensing of hydrogen embrittlement process of austenitic stainless steel support project". This work was also supported by JSPS KAKENHI Grant Number 19KK0095, 19K21910, and 21H04592, and JST FOREST program (Grant Number JPMJFR2023, Japan).

References

[1] H. Barthelemy, M. Weber, F. Barbier, “Hydrogen storage: Recent improvements and industrial perspectives,” International Journal of Hydrogen Energy, 42, 11, (2017), 7254–7262.

[2] Y. Ogawa, S. Okazaki, O. Takakuwa, H. Matsunaga, “The role of internal and external hydrogen in the deformation and fracture processes at the fatigue crack tip zone of metastable austenitic stainless steels,” Scripta Materialia, 157, (2018), 95–99.

[3] L. Zhang, M. Wen, M. Imade, S. Fukuyama, K. Yokogawa, “Effect of nickel equivalent on hydrogen gas embrittlement of austenitic stainless steels based on type 316 at low temperatures,” Acta Materialia, 56, 14, (2008), 3414–3421.

[4] Y. Murakami, T. Kanezaki, Y. Mine, S. Matsuoka, “Hydrogen Embrittlement Mechanism in Fatigue of Austenitic Stainless Steels,” Metall. Mater. Trans. A, 39, 6, (2008), 1327–1339.

[5] G. Han, J. He, S. Fukuyama, K. Yokogawa, “Effect of stain-induced

martensite on hydrogen environment embrittlement of sensitized austenitic stainless steels at low temperature," Acta Materialia, 46, (1998), 4559–4570.

[6] M. Wang, C. C. Tasan, M. Koyama, D. Ponge, D. Raabe, "Enhancing Hydrogen Embrittlement Resistance of Lath Martensite by Introducing Nano-Films of Interlath Austenite", Metallurgical and Materials Transactions A, 46, (2015), 3797–3802.

[7] L. Zhang, M. Imade, B. An, M. Wen, T. Iijima, S. Fukuyama, K. Yokogawa, "Internal reversible hydrogen embrittlement of austenitic stainless steels based on type 316 at low temperatures," ISIJ International, 52, 2, (2012), 240–246.

[8] S. Matsuoka, J. Yamabe, H. Matsunaga, "Criteria for determining hydrogen compatibility and the mechanisms for hydrogen-assisted, surface crack growth in austenitic stainless steels," Engineering Fracture Mechanics, 153, (2016), 103–127.

[9] Y. Sekine, H. Soyama, "Evaluation of equibiaxial compressive stress introduced into austenitic stainless steel using an eddy current method," Journal of Nondestructive Evaluation, 31, 2, (2012), 99–107.

[10] T. Uchimoto, T. Takagi, X. Wu, H. Feng, R. Urayama, "Changes in eddy current testing signals of fatigue cracks by heat pro-cessing," International Journal of Applied Electromagnetics and Mechanics, Vol. 52, No. 1-2 (2006), pp. 677-684.

[11] T. Uchimoto, T. Takagi, K. Ohtaki, Y. Takeda, A. Kawakami, "Electromagnetic modeling of fatigue cracks in plant environment for eddy current testing," International Journal of Applied Electromagnetics and Mechanics, 39, (2012), 261–268.

[12] M. Shaira, P. Guy, J. Courbon, N. Godin, "Monitoring of martensitic transformation in austenitic stainless steel 304L by eddy currents," Research in Nondestructive Evaluation, 21, 2, (2010), 112–126.

[13] E. Tokuda, S. Takeda, T. Uchimoto, T. Takagi, H. Enoki, T Iijima, "Evaluation of the Hydrogen Embrittlement on the Hydrogen Exposed Austenitic Stainless Steel Fatigue Specimens by Eddy Current Testing," Proceeding of the 19th International Symposium on Applied Electromagnetics and Mechanics, (2019), China, 292.

[14] W. Cheng, Eddy Current Examination of Fatigue Crack in Inconel Welds, Journal of Pressure Vessel Technology, Vo. 129(2007), 169–174.

[15] N. Yusa, L. Janousek, Z. Chen, K. Miya, "Diagnostics of stress corrosion and fatigue cracks using benchmark signals," Materials Letters, 59, 28, (2005), 3656–3659.

[16] Blitz J, Simpson G. Ultrasonic Methods of Non-destructive Testing. Springer; 1995.

[17] Schmerr LW. Fundamentals of Ultrasonic Phased Arrays. vol. 215. Cham: Springer International Publishing; 2015. https://doi.org/10.1007/978-

3-319-07272-2.

[18] Jhang K-Y, Lissenden CJ, Solodov I, Ohara Y, Gusev V. Measurement of Nonlinear Ultrasonic Characteristics. Springer Singapore; 2020. https://doi.org/10.1007/978-981-15-1461-6.

[19] Remillieux MC, Kaoumi D, Ohara Y, Stuber Geesey MA, Xi L, Schoell R, et al. Detecting and imaging stress corrosion cracking in stainless steel, with application to inspecting storage canisters for spent nuclear fuel. NDT E Int 2020;109:102180-1–17. https://doi.org/10.1016/j.ndteint.2019.102180.

[20] Ohara Y, Mihara T, Sasaki R, Ogata T, Yamamoto S, Kishimoto Y, et al. Imaging of closed cracks using nonlinear response of elastic waves at subharmonic frequency. Appl Phys Lett 2007;90:011902-1–3. https://doi.org/10.1063/1.2426891.

[21] Horinouchi S, Ikeuchi M, Shintaku Y, Ohara Y, Yamanaka K. Evaluation of closed stress corrosion cracks in Ni-based alloy weld metal using subharmonic phased array. Jpn J Appl Phys 2012;51:07GB15-1–5. https://doi.org/10.1143/JJAP.51.07GB15.

[22] Ohara Y, Takahashi K, Murai S, Yamanaka K. High-selectivity imaging of closed cracks using elastic waves with thermal stress induced by global preheating and local cooling. Appl Phys Lett 2013;103:031917-1–5. https://doi.org/10.1063/1.4816160.

[23] Haupert S, Ohara Y, Carcreff E, Renaud G. Fundamental wave amplitude difference imaging for detection and characterization of embedded cracks. Ultrasonics 2019;96:132–9. https://doi.org/10.1016/j.ultras.2019.02.003.

[24] Ohara Y, Nakajima H, Haupert S, Tsuji T, Mihara T. Nonlinear ultrasonic phased array with fixed-voltage fundamental wave amplitude difference for high-selectivity imaging of closed cracks. J Acoust Soc Am 2019;146:266–77. https://doi.org/10.1121/1.5116017.

[25] Ohara Y, Haupert S, Li S. Ultrafast phased-array imaging with pump excitation for closed-crack imaging. Appl Phys Express 2021;14:126505-1–5. https://doi.org/10.35848/1882-0786/ac3d1e.

[26] T. Uchimoto, P. Guy, T. Takagi, J. Courbon, “Evaluation of an EMAT–EC dual probe in sizing extent of wall thinning,” NDT&E International, 62, (2014), 160–166.

[27] T. Uchimoto, T. Takagi, T. Ichihara, G. Dobmann, “Evaluation of fatigue cracks by an angle beam EMAT–ET dual probe,” NDT&E International, 72, (2015), 10–16.

[28] American Society of Testing and Marterials (ASTM), Standard test method for measurement of fatigue crack growth (E647), ASTM 2011.

[29] H. Fukutomi, T. Takagi, J. Tani, A Meshless Finite Element Method for Modeling Coils and Cracks to Simulate Eddy Cur-rent Testing,

Transactions of the Japan Society of Mechanical Engineers Series A, Vol.64, No.622 (1998), pp.1541-1547.

[30] Ohara Y, Oshiumi T, Nakajima H, Yamanaka K, Wu X, Uchimoto T, et al. Ultrasonic phased array with surface acoustic wave for imaging cracks. AIP Adv 2017;7:065214-1–7. https://doi.org/10.1063/1.4989725.

[31] Ohara Y, Nakajima H, Tsuji T, Mihara T. Nonlinear surface-acoustic-wave phased array with fixed-voltage fundamental wave amplitude difference for imaging closed cracks. NDT E Int 2019;108:102170-1–10. https://doi.org/10.1016/j.ndteint.2019.102170.

[32] Ohara Y, Oshiumi T, Wu X, Uchimoto T, Takagi T, Tsuji T, et al. High-selectivity imaging of the closed fatigue crack due to thermal environment using surface-acoustic-wave phased array (SAW PA). Ultrasonics 2021;119:106629-1–8. https://doi.org/10.1016/j.ultras.2021.106629.

[33] Ohara Y, Mihara T, Yamanaka K. Subharmonic Phased Array for Crack Evaluation (SPACE). Nonlinear Ultrason. Vibro-Acoustical Tech. Nondestruct. Eval., Springer; 2019, p. 419–69. https://doi.org/10.1007/978-3-319-94476-0_10.

[34] Ohara Y, Nakajima H, Haupert S, Tsuji T, Mihara T. Imaging of three-dimensional crack open/closed distribution by nonlinear ultrasonic phased array based on fundamental wave amplitude difference. Jpn J Appl

Phys 2020;59:SKKB01-1–9. https://doi.org/10.35848/1347-4065/ab79ea.

List of Abbreviations

- ECT: Eddy current testing
- UT: Ultrasonic testing
- PA: Phased array
- EBSP: Electron Backscatter Pattern